International Journal of Multiphase Flow 35 (2009) 427–438

Contents lists available at ScienceDirect

International Journal of Multiphase Flow

journal homepage: www.elsevier.com/locate/ijmulflow

On the quenching of steel and zircaloy spheres in water-based nanofluids with alumina, silica and diamond nanoparticles

Hyungdae Kim, Gregory DeWitt, Thomas McKrell, Jacopo Buongiorno *, Lin-wen Hu

Massachusetts Institute of Technology, Cambridge, MA 02139, USA

ARTICLE INFO

Article history:
Received 20 November 2008
Received in revised form 4 February 2009
Accepted 10 February 2009
Available online 21 February 2009

Keywords:
Film boiling
Minimum heat flux
Wettability
Rodlets

ABSTRACT

The quenching curves (temperature vs time) for small (~1 cm) metallic spheres exposed to pure water and water-based nanofluids with alumina, silica and diamond nanoparticles at low concentrations (≤0.1 vol%) were acquired experimentally. Both saturated ($\Delta T_{sub} = 0$ °C) and highly subcooled ($\Delta T_{sub} = 70$ °C) conditions were explored. The spheres were made of stainless steel and zircaloy, and were quenched from an initial temperature of ~1000 °C. The results show that the quenching behavior in nanofluids is nearly identical to that in pure water. However, it was found that some nanoparticles accumulate on the sphere surface, which results in destabilization of the vapor film in subsequent tests with the same sphere, thus greatly accelerating the quenching process. The entire boiling curves were obtained from the quenching curves using the inverse heat transfer method, and revealed that alumina and silica nanoparticle deposition on the surface increases the critical heat flux and minimum heat flux temperature, while diamond nanoparticle deposition has a minimal effect on the boiling curve. The possible mechanisms by which the nanoparticles affect the quenching process were analyzed. It appears that surface roughness increase and wettability enhancement due to nanoparticle deposition may be responsible for the premature disruption of film boiling and the acceleration of quenching. The basic results were also confirmed by quench tests with rodlets.

1. Introduction

Quenching refers to the rapid cooling of a very hot solid object by exposure to a much cooler liquid. Quenching phenomena occur in nature and industry. For example, when molten lava is spewed from an undersea volcanic eruption, it is quenched by the surrounding water. Humans have been relying on quenching in the making of metal objects for centuries. It is well known that steels can be hardened by heating and subsequent rapid cooling, a process that is done by immersion in water (hard quench) or oils (slow quench). Flash freezing of food can be done by quenching it in liquid carbon dioxide (dry ice). Quenching also plays an important role in mitigating the consequences of loss-of-coolant accidents in nuclear reactors. And the list goes on.

The heat transfer rate during the quenching process is limited by the occurrence of film boiling, in which a stable vapor film blankets the surface of the hot object, thus creating a very high resistance to energy transfer. An acceleration of the transition from film boiling to nucleate boiling is often desirable, as it results in a much higher heat transfer rate. Dispersing nanoparticles in water could be a means to accelerate that transition and, more generally, enhance heat transfer during the quenching process, as explained next.

The dispersion of nanoparticles in water realizes a so-called nanofluid. The general boiling behavior of nanofluids has been studied for a few years now. A number of investigations showed that nanofluids can effectively delay departure from nucleate boiling (DNB) with respect to pure fluids (You et al., 2003; Vassallo et al., 2004; Bang and Chang, 2005). It was found that nanoparticle deposition on the boiling surface can occur, which significantly roughens the surface itself (Milanova and Kumar, 2005; Kim et al., 2006a,b, 2007a; Liu and Liao, 2008). Moreover, the deposition of oxide nanoparticles like alumina and titania appeared to enhance the wettability of the boiling surface significantly (Kim et al., 2007a,b, 2006c). These changes alter the nucleate boiling heat transfer characteristics of the surface and, specifically, are thought to be responsible for the enhancement of the DNB heat flux (or critical heat flux, CHF).

On the other hand, as of today only three publications exist concerning the *quenching* behavior of nanofluids. First, Park et al. (2004) performed quenching experiments of a high-temperature copper sphere in alumina nanofluids to investigate the effect of the nanoparticles on film boiling heat transfer. The nanoparticle concentration in their experiments was very high (from 5 to 20 vol%), and a subcooling range from 20 to 80 K was explored. Their results showed that the film boiling heat transfer rate in nanofluids was actually somewhat *lower* than in pure water. In addition, they observed an intriguing phenomenon: quenching of

* Corresponding author. Tel.: +1 617 253 7316.
E-mail address: jacopo@mit.edu (J. Buongiorno).

0301-9322/$ - see front matter © 2009 Elsevier Ltd. All rights reserved.
doi:10.1016/j.ijmultiphaseflow.2009.02.004

a sphere previously quenched in the nanofluid, was much more rapid than quenching of a fresh (clean) sphere. They hypothesized that nanoparticle deposits on the previously-quenched sphere prevent formation of a stable vapor film on the sphere surface, thus bypassing the film boiling regime altogether. The second publication is by Xue et al. (2007), who carried out quenching experiments of a nickel-plated copper sphere in a pool of water-based nanofluids containing carbon nanotubes (CNT). Based on the assumption that the copper sphere could be thermally lumped, they obtained boiling curves from the temperature-time history of the sphere, using the transient calorimeter technique. Their boiling curves suggested that the CNT nanofluids yield an enhanced CHF, transition boiling heat transfer rate, and minimum heat flux (Leidenfrost point) as compared to water. They also found that the wettability of the sphere surface improved due to the surfactant used in the preparation of the CNT nanofluids, and that the CNT deposited on the surface during quenching. Third, Choo et al. (2008) investigated the quenching characteristics of water and water-based nanofluids with silicon nanoparticles using a bare platinum wire and a silicon nanoparticle-coated platinum wire. The latter was prepared by boiling a bare platinum wire in the silicon nanofluid. No meaningful differences in the boiling heat transfer characteristics between water and the silicon nanofluid were observed during the experiments with the bare wire. However, a considerably higher heat transfer coefficient was obtained with the nanoparticle-coated wire in the nucleate and the transition boiling regions.

The Massachusetts Institute of Technology is investigating the use of nanofluids in safety systems for light water nuclear reactors (Buongiorno et al., 2008; Chupin et al., 2008). Shortly after a hypothetical loss of coolant accident in such reactors, the fuel can reach very high temperatures (>1000 °C). The emergency core cooling system, which injects cold water in the reactor core, is immediately actuated to reduce the fuel temperature. Fuel cooling occurs slowly through the development of a quench front which advances upward in the core. The speed of the quench front and thus the peak fuel temperature reached during the accident depend on a combination of factors including, among others, film boiling heat transfer and wettability of the fuel surface. The use of nanofluids potentially could afford a significant increase of the quench front speed, and thus an improvement of the safety performance of the reactors. As a first step in the merit assessment of nanofluids for use in nuclear reactors, the quenching characteristics of small metallic spheres were studied, and the results are reported in this paper. The experimental apparatus and procedures are described in Section 2. The quenching and boiling curves are reported in Sections 3 and 4, respectively, while the data are interpreted in Section 5.

2. Experimental

2.1. Preparation and characterization of nanofluids

We have selected three nanoparticle materials for this study, i.e., alumina (Al_2O_3), silica (SiO_2), and diamond (C). Water-based nanofluids of these three materials were purchased from Nyacol (alumina), Sigma–Aldrich (silica), and PlasmaChem (diamond). The vendor-specified concentrations of the nanofluids were 20%, 34%, and 4% by weight, respectively. The as-purchased nanofluids were then diluted with deionized water to the low concentrations of interest for the quenching experiments, i.e., 0.001%, 0.01%, and 0.1% by volume. For practical applications a low particle concentration is very desirable, as the properties of the dilute nanofluids (particularly viscosity) stay similar to those of water, and the nanofluids typically remain transparent. The size (effective diameter) of the nanoparticles in the dilute nanofluids was measured with the dynamic light scattering (DLS) technique (see Fig. 1a), and the averaged diameter was found to be 38.8 nm for alumina, 32.9 nm for silica, and 165.4 nm for diamond, respectively. The nanoparticles were visualized with transmission electron microscopy (TEM) or scanning electron microscopy (SEM) to reveal their shape. As seen in Fig. 1b, the individual particle size of the alumina and

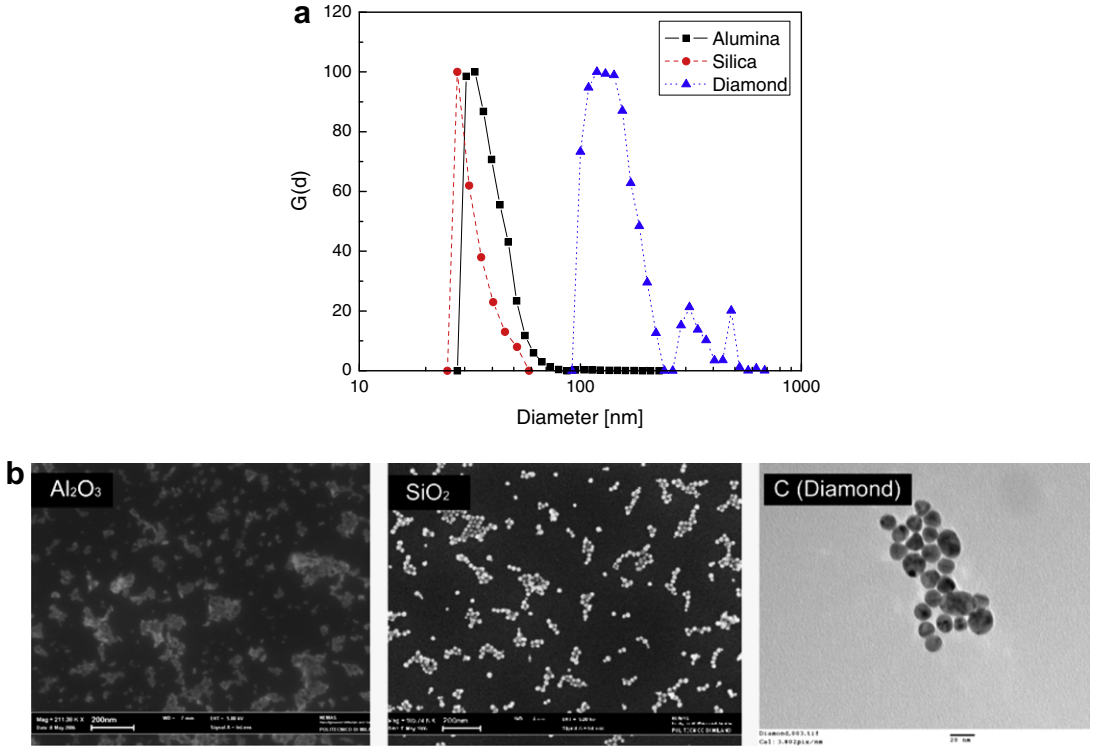

Fig. 1. (a) Size distribution of alumina, silica, and diamond nanoparticles in nanofluids as measured by DLS. (b) transmission electron microscopy (TEM) and scanning electron microscopy (SEM) images of dry nanofluid samples.

silica seems consistent with the results of the DLS measurements, which is an indication of good nanoparticle dispersion in those nanofluids. But in the case of diamond the individual nanoparticles in the TEM image have a smaller diameter than the DLS result, which suggests the presence of particle agglomerates in the diamond nanofluids.

Various properties relevant to two-phase heat transfer were also measured or estimated. The surface tension, thermal conductivity and viscosity of the nanofluids were measured by means of a Sigma 703 tensiometer, a KD2 thermal conductivity probe and a capillary viscometer, respectively. The nanofluid density was calculated as $\rho_p\varphi + \rho_f(1-\varphi)$, where φ is the nanoparticle volumetric fraction, and ρ_p and ρ_f are the density of the nanoparticle material and base fluid, respectively. The nanofluid heat capacity was estimated as $[\rho_p c_p\varphi + \rho_f c_f(1-\varphi)]/[\rho_p\varphi + \rho_f(1-\varphi)]$, where c_p and c_f are the specific heat of the nanoparticle material and base fluid, respectively, as recommended by Zhou and Ni (2008). All the nanofluid properties were found to be within ±5% of those of pure water, which is not surprising, given the low concentration of nanoparticles used in our experiments. As such, thermo-physical properties effects are not expected to be significant in our experiments.

2.2. Apparatus

Fig. 2 shows a schematic and photograph of the experimental setup for the quench tests. It consists of the test sample (sphere), the furnace, the air slide, the quench pool, and the data acquisition system. A radiant furnace with a maximum temperature of 1500 °C is used to heat the test sample. A DC power supply (25 V, 150 A) is used to power the furnace. A B-type sheathed thermocouple is mounted inside the furnace to monitor the temperature. A pneumatic air slide moves the test sample between the furnace and the pool with the stroke length of 200 mm. Pressurized air near 600 kPa is used to operate the slide. The average downward velocity of the sample is about 0.5 m/s, which is measured with a high-speed camera. The time to move the heated sample from the furnace to the pool is about 0.4 s. A 4-way solenoid valve is adopted to change the direction of the slide. The quench pool is 95 mm × 95 mm rectangular vessel having depth of 150 mm, which has an effectively infinite thermal capacity with respect to the test sample. It is made of Pyrex glass for visual observation of the quenching phenomena. The pool is placed on a hot plate with a maximum power of 800 W. The temperature of the quench pool is maintained with a feedback control of the hot plate and a Pt-100 ohm RTD sensor immersed in the pool. A HP Agilent 34980A data acquisition system and a PC are used for gathering and storing temperature data from the thermocouple within the test sample. The temperature data is acquired at a rate of 10 Hz which is fast enough to capture all the transitions in the quenching curve accurately. Visualization of the quenching process phenomena is carried out by a high speed CMOS camera (Vision Research Phantom V7.1) which is capable of capturing 4800 fps at the full 800 × 600 pixel resolution.

2.3. Test sample

Fig. 3 shows the details of the test samples for the quenching experiment. The test sample consists of a metal sphere, a thermocouple to record the temperature at the center of the sphere, and a reinforcing precision tube to mechanically support them. The sphere materials selected for this study are stainless steel (SS) and zircaloy (Zry), a zirconium-based alloy used as cladding material in the fuel rods of nuclear reactors. The thermophysical properties for these materials are reported in Table 1. SS spheres of 9.5-mm diameter were purchased from McMaster-Carr, while Zry

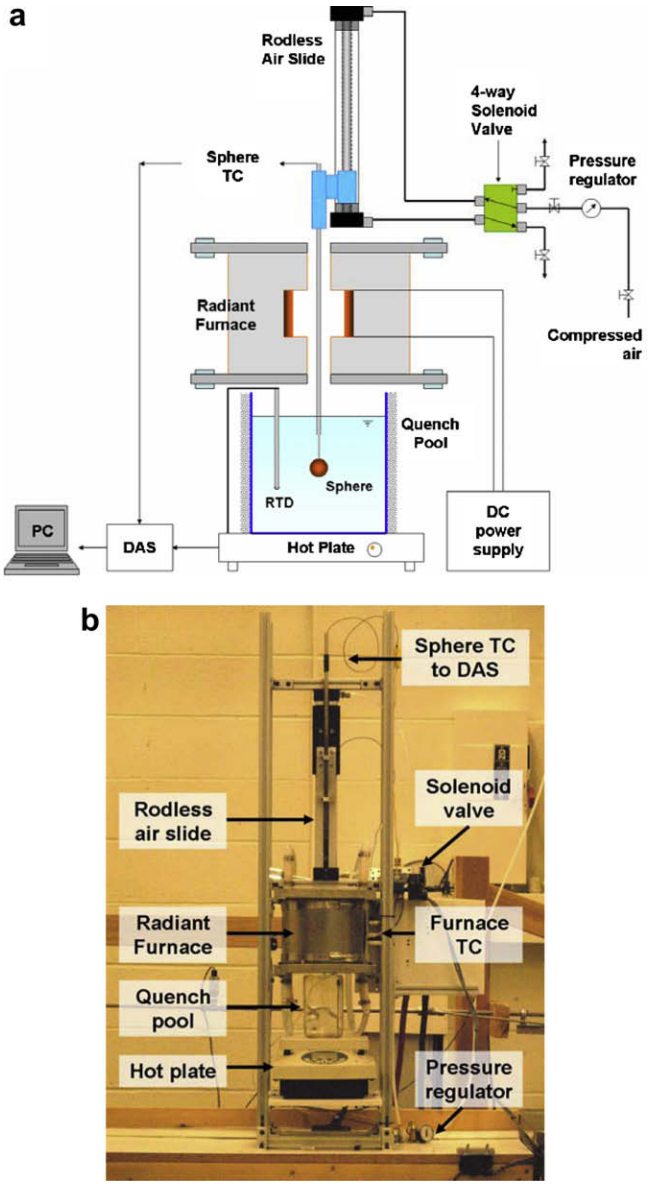

Fig. 2. Experimental apparatus: (a) schematic diagram, (b) photograph.

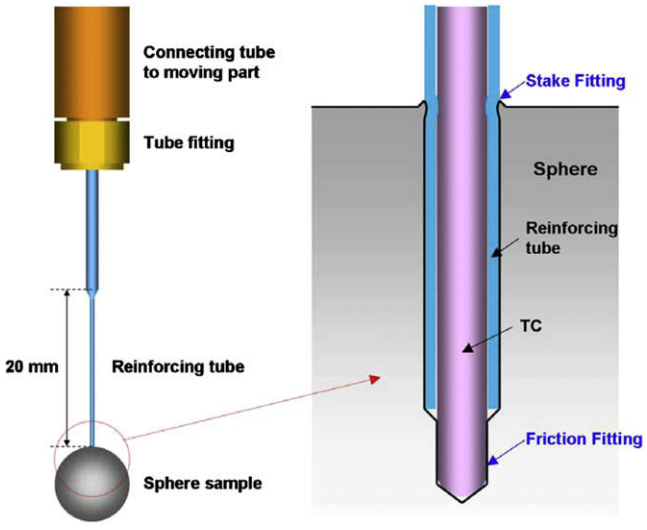

Fig. 3. Test sample assembly (not to scale).

Table 1
Thermal properties of stainless steel (grade 302) and zircaloy.

Temperature	Density (kg/m^3)		Thermal conductivity (W/m K)		Specific heat (J/kg K)	
	SS	Zry	SS	Zry	SS	Zry
27 °C	8000	6550	12.5	12.6	480	284
400 °C	7850	6516	18.6	16.6	568	322
800 °C	7679	6479	25.5	22.7	614	368

spheres of 10-mm diameter were supplied by AREVA, a sponsor of ours. Their as-received surface roughness is 0.6 μm and 3.1 μm, respectively. Each sphere is drilled to the center creating a hole stepped from 0.9 mm to 0.5 mm in diameter. A 0.5-mm diameter K-type sheathed ungrounded thermocouple with the measurement uncertainty of ±1 °C is inserted to the bottom of the hole by friction fitting. This technique ensures a good thermal contact with the sphere, and thus minimizes the thermocouple response time, so the rapidly-varying temperature of the sphere can be acquired correctly. A reinforcing tube of 0.6 mm ID and 0.89 mm OD is inserted between the 0.5-mm diameter thermocouple and the 0.9-mm diameter hole to mechanically support the test sample. A staking technique – hitting the edge with a sharp tool – is used to connect the tube and the sphere (see Fig. 3). The reinforcing tube is connected to the main connecting tube via a tube fitting.

The reinforcing tube is a path of conduction heat loss during the experiments, which should be minimized. The ratio of the reinforcing tube diameter to that of the sphere is very low (0.09), so conduction losses are negligible. The length of the tube is also an important design parameter because vigorous boiling on the sphere surface causes the sphere to vibrate, which may affect boiling itself. Based on an analysis of mechanical vibration of the rod–sphere system, the length of the precision tube was selected to be 20 mm.

2.4. Experimental procedure

A fresh sphere is thoroughly rinsed with acetone, ethanol, and distilled water before every quenching test. The test sphere is heated up to the initial temperature (~1030 °C) in the radiant furnace, and then is plunged into the quench pool with an immersion depth of 6 cm, where the boiling phenomena occurring on the sphere should not be influenced by wavy motion of the free liquid surface due to vigorous vapor flow. The temperature–time history of the sphere is acquired during the cooldown. When the sphere has reached thermal equilibrium with the quench pool, the test is over. The same sphere can be reheated and re-quenched, to investigate the effect of surface changes that may have occurred during the previous quench test. This process has been repeated up to seven times, as will be explained in the next section. Pure water and nanofluids are used as the cooling liquid at saturated and highly subcooled (ΔT_{sub} = 70 °C), always at atmospheric pressure.

3. Results

3.1. Saturated test results

Fig. 4 shows a typical temperature–time history (quenching curve) of a SS sphere quenched in saturated water without nanoparticles. The temperature of the quenched sphere decreases experiencing various heat transfer modes, i.e., film boiling, transition boiling, nucleate boiling, and natural convection. The general shape of the quenching curve can be predicted qualitatively from a simple energy balance for the sphere:

$$\rho c V \frac{d\Delta T}{dt} = -q'' S \tag{1}$$

where ρ and c are the sphere density and specific heat, respectively, V and S are the sphere volume and surface area, respectively, ΔT is

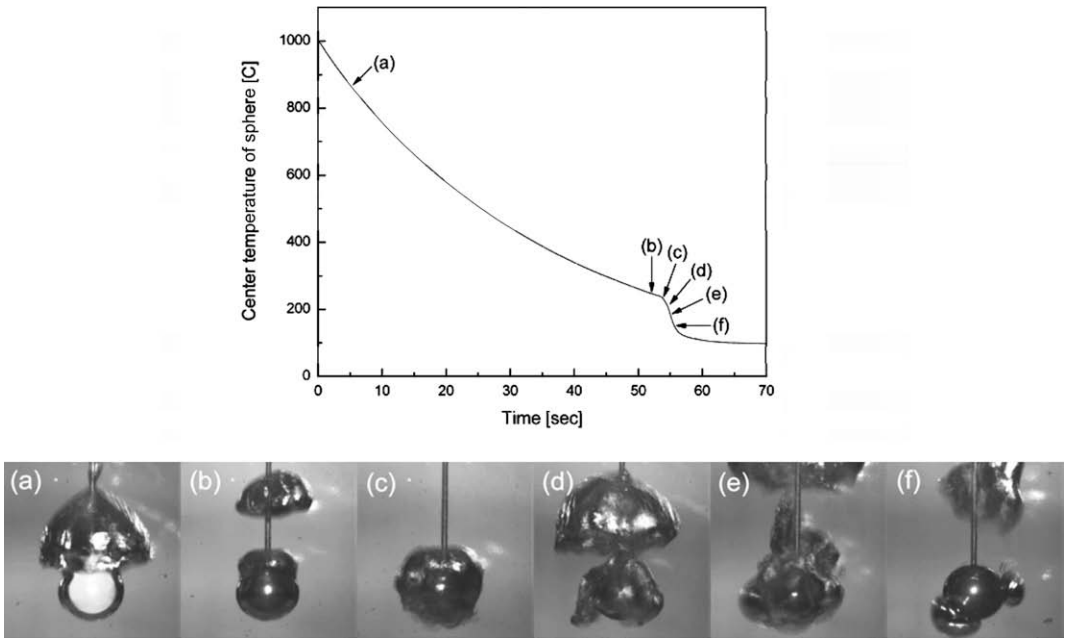

Fig. 4. Typical temperature–time history and quenching boiling phenomena on a SS sphere in pure water at saturated condition.

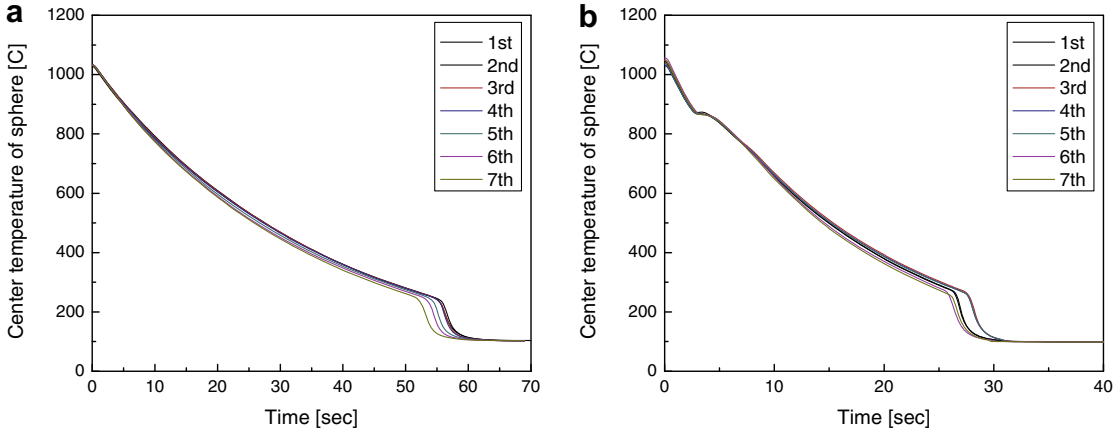

Fig. 5. Cooling curves for repetitive runs of (a) SS sphere and (b) Zry sphere in pure water at saturated condition.

the temperature difference between the sphere and the pool, and $q''(\Delta T)$ is the heat flux at the surface of the sphere at ΔT. Differentiating Eq. (1) with respect to time, one gets:

$$\frac{d^2\Delta T}{dt^2} = \frac{S}{\rho c V}\frac{dq''}{d\Delta T}\cdot\left(-\frac{d\Delta T}{dt}\right) \tag{2}$$

Since the sphere is cooling down, the factor $\left(-\frac{d\Delta T}{dt}\right)$ is always positive, thus the curvature of the quenching curve depends only on the slope of the heat flux curve with respect to temperature. Note that $q''(\Delta T)$ is the boiling curve, therefore we have the following:

- The initial section of the quenching curve corresponds to film boiling and thus has a positive curvature.
- The minimum heat flux (MHF) point, or Leidenfrost point, is where the quenching curve has its first inflection point.
- Transition boiling corresponds to the section of the curve with negative curvature.
- The CHF point corresponds to the second inflection point.
- The final section of the quenching curve represents nucleate boiling and natural convection, and has a positive curvature.

The various heat transfer regimes were recorded with the video camera, and the results are shown in Fig. 4. In film boiling the sphere is completely blanketed with the stable vapor film, as seen in frame (a). As the sphere temperature decreases, the vapor film becomes thinner but remains stable (frame (b)). The MHF point is shown in frame (c), and marks the start of transition boiling, which is shown in frames (c) and (d). Note that some areas of the sphere surface are in contact with the liquid while some are still covered with the vapor film. This behavior is typical of transition boiling. The CHF point is shown in frame (e), and marks the start of the nucleate boiling regime. Note the vigorous boiling action here. Finally, as the sphere temperature asymptotically converges to the temperature of the surrounding liquid, the number of bubbles produced at the surface decreases, as seen in frame (f), until the bubbles disappear completely, which signals the occurrence of single-phase convective heat transfer.

Prior to the nanofluid tests, repeated quench tests were performed in pure water, to establish the base cases. Fig. 5 shows the results of these initial tests with both a SS sphere and a Zry sphere.[1] It can be seen that the quenching curve is reasonably repeatable with some minor data scattering in the transition and nucleate boiling regions, likely due to the effect of surface oxidation under repeated heating and quenching cycles from >1000 °C to room temperature. The brief plateau at high temperature in the quenching curves of the Zry spheres is due to a specific heat spike corresponding to the transition from the beta to alpha phase of zirconium, which occurs at around 860 °C (Terai et al., 1997). Also, it can be noted that the quenching test duration for Zry spheres is roughly half that of SS spheres, which is due to the different thermal capacity (ρc) of the materials, i.e., $\sim 2 \times 10^6$ J/m^3 K for Zry vs $\sim 4 \times 10^6$ J/m^3 K for SS.

Fig. 6 shows the SS sphere quenching curves for alumina nanofluids at different concentrations (0.001%, 0.01%, and 0.1% by volume) and, at each concentration, for subsequent repetitions. All the curves for the lowest concentration nanofluid fall within the data scattering of the pure water reference case. At the higher concentrations the curves from the first run also overlap with the water data. This suggests that the nanoparticles present in the fluid have little or no effect on the quenching behavior of a fresh sphere. However, the curves from the subsequent repetitions exhibit a dramatic shift to the left. That is, the end of film boiling occurs significantly earlier in the process and at a significantly higher temperature. The shift is strongest at the highest nanoparticle concentration (0.1 vol%) and grows with each repetition. Finally the quenching duration in the seventh test at 0.1 vol% is shortened to about 50% of the typical time required to cool the hot sphere in pure water. High speed visualization of the seventh run at 0.1 vol% (see Fig. 6d) reveals an interesting fact: nucleation of vapor bubbles intermittently occurs at high temperatures, with readings from the thermocouple in the center of the sphere as high as 450 °C, which are typically associated with the stable film boiling region. Such intermittent nucleation of bubbles disrupts the vapor film around the sphere and promotes early cooling of the hot sphere, which is consistent with the quenching curve data.

Fig. 7 shows the quenching curves of SS and Zry spheres for alumina, silica and diamond nanofluids (all at 0.1 vol% concentration). While the results obtained with the two different sphere materials show qualitatively identical trends for the same nanoparticle material, the quenching acceleration strongly depends on the nanoparticle material used. Specifically, the diamond nanofluid does not accelerate the quenching process nearly as much as alumina and silica nanofluids do.

3.2. Subcooled test results

Fig. 8 shows the pure water results for a pool temperature of 30 °C (i.e., 70 °C subcooling) for both SS and Zry spheres. The end of film boiling, or MHF, occurs over a broad range of temperature readings, between 250 °C and 400 °C for SS sphere and between

[1] The temperature uncertainty in this plot and all other quenching curves throughout the paper is ±1 °C. Error bars were omitted because they would render the figures illegible.

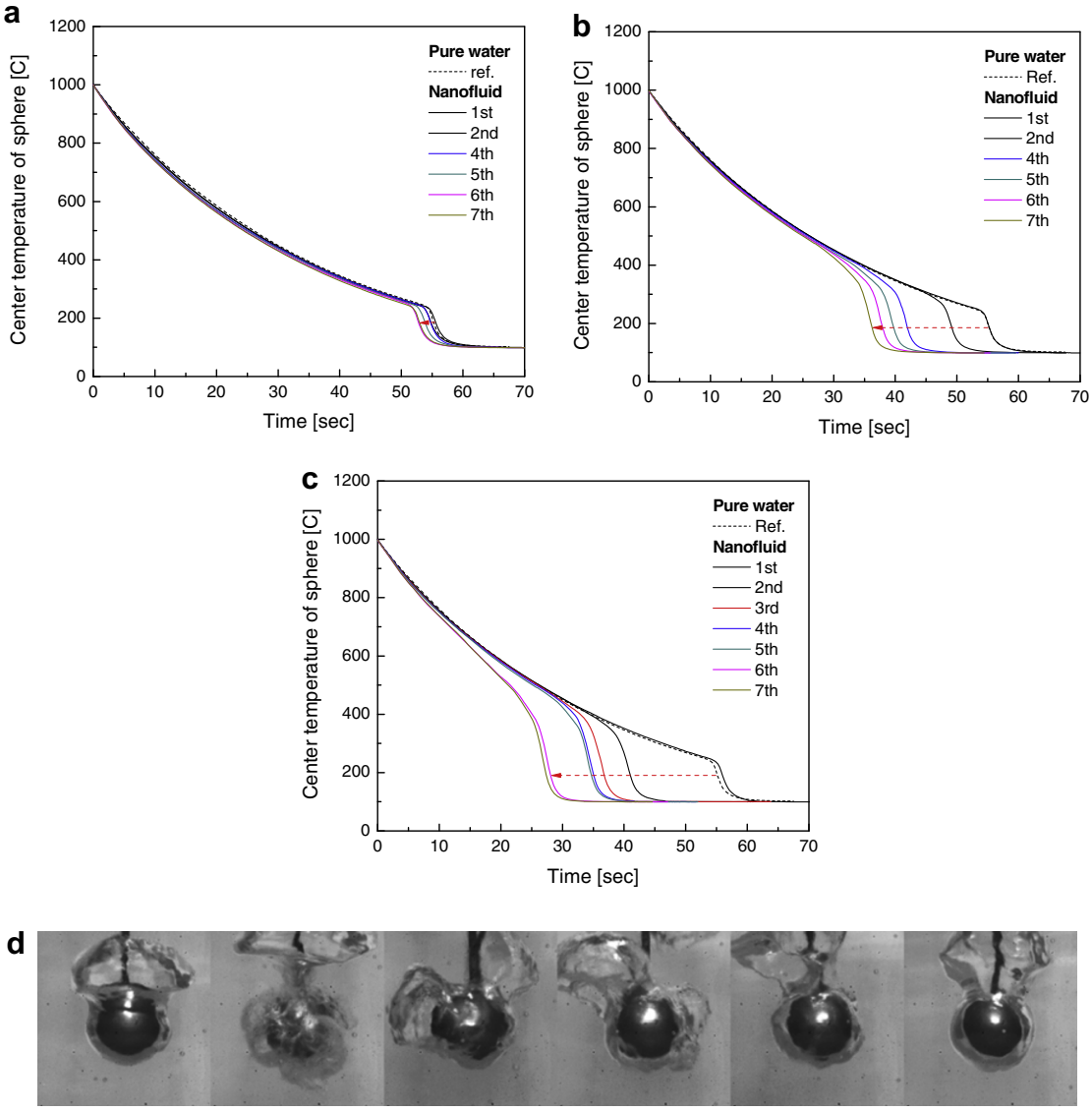

Fig. 6. Quenching curves for SS sphere repetitive runs in alumina nanofluids of (a) 0.001, (b) 0.01, and (c) 0.1 vol% concentration at saturated condition, and (d) photographs of intermittent bubble nucleation in the film boiling region near 22 s after the start of the 7th run for the 0.1 vol% nanofluid. The time interval between frames is 20 ms.

300 °C and 450 °C for Zry sphere. As noted by Nishio et al. (1987), there are two different collapse modes of the vapor film in subcooled film boiling: a coherent collapse mode in which the vapor film collapses simultaneously over the entire heat transfer surface, and a propagative collapse mode in which a precursory local collapse of the vapor film propagates across the heat transfer surface. Compared with the coherent collapse mode, the propagative collapse mode occurs at higher temperatures and the corresponding MHF wall superheat is more sensitive to various system parameters, including the oxidation status of the surface, the roughness, etc. Thus the MHF data scattering in our subcooled experiments might be due to some of these poorly controlled parameters. However, the effect of the nanoparticles on the MHF point is well beyond the data scattering of pure water, as explained next.

The results for SS spheres quenched in alumina nanofluids at subcooled conditions are shown in Fig. 9. The curves for the 0.001 and 0.01 vol% nanofluids are similar to that of pure water, within the data scattering observed in the subcooled water tests. However, the quenching process is significantly accelerated during the first repetition with the 0.1 vol% nanofluid. In this particular test the sphere temperature drops very fast, apparently bypassing the slow cooldown behavior typical of film boiling. This observation is consistent with Park et al. (2004) regarding their 'unwashed sphere'. The visualization of the process shows that soon after the sphere is immersed in the fluid, the vapor film starts to collapse from the bottom of the sphere and it propagates up the sphere surface, bringing about the total collapse of the vapor film within 1.2 s (see Fig. 9d). Such rapid quenching behavior is observed in the following repetitions as well. This trend is seen clearly in silica nanofluids also, but very weakly in diamond nanofluids, as shown in Fig. E.A.1 in the Electronic Annex in the online version of this article.

4. Boiling curves

The boiling curves – surface heat flux vs surface temperature – were obtained from the quenching curves using the inverse heat transfer method, as explained in the Appendix A (see Electronic Annex in the online version of this article). In the next section the various segments of the boiling curve are analyzed in some details, and the differences between water and the nanofluids highlighted.

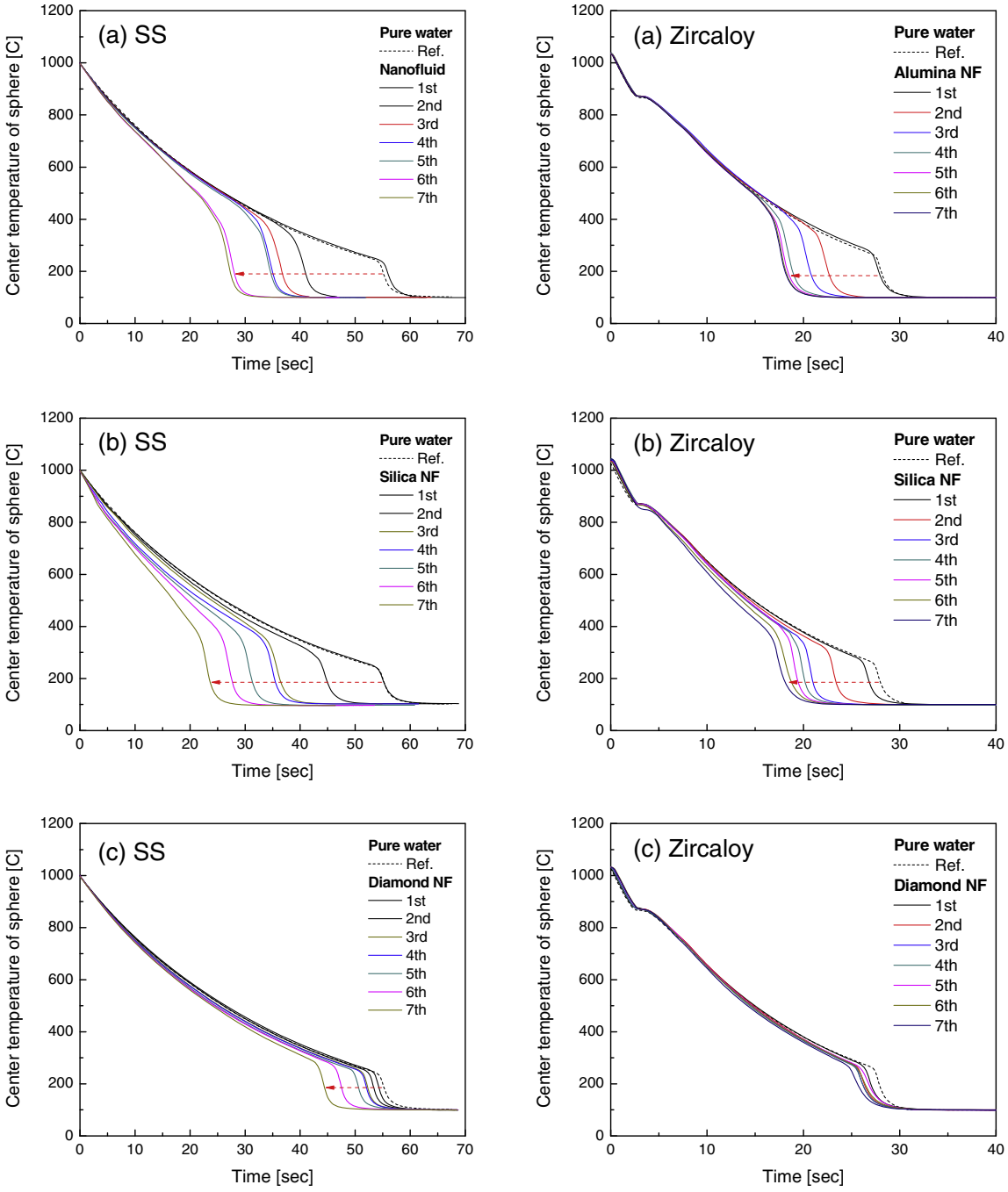

Fig. 7. Quenching curves for SS (left) and Zry (right) spheres in 0.1 vol% (a) alumina, (b) silica, and (c) diamond nanofluids at saturated conditions.

4.1. Film boiling

The surface heat flux measured in the film boiling region is reported in Fig. 10. In this figure, the measured heat flux is also compared with the *total* heat flux calculated with the film boiling heat transfer correlations of Bromley et al. (1953) and Michyosi et al. (1988) for saturated and subcooled conditions, respectively, including the effect of radiation heat transfer:

$$q''_{total} = q''_{film} + Jq''_{rad} \tag{3}$$

where the radiant factor J is 7/8 for a sphere in the case of pool film boiling and $q''_{rad} = \varepsilon\sigma(T_w^4 - T_f^4)$ with $\varepsilon = 0.6$ for a moderately oxidized metal sphere (Liu, 1995). Fig. 10 shows that the film boiling heat transfer rates are almost identical for all fluids, at both saturated and subcooled conditions, and the data are in good agreements with the predictions of the Bromley's and Michyoshi's correlations. This finding suggests that the nanoparticles present in the fluids have no significant effect on film boiling heat transfer.

4.2. Critical heat flux (CHF) and minimum heat flux (MHF) points

Fig. 11 shows the boiling curves for the SS spheres quenched in pure water and nanofluids at saturated conditions. Similar curves for the Zry spheres are reported in Fig. E.A.2 in the Electronic Annex. Note that the CHF values for saturated water obtained in our experiments are significantly lower than the values predicted by Zuber's popular CHF correlation (corrected for spherical effects, as recommended by Collier and Thome, 1996), ~1400 kW/m^2. However,

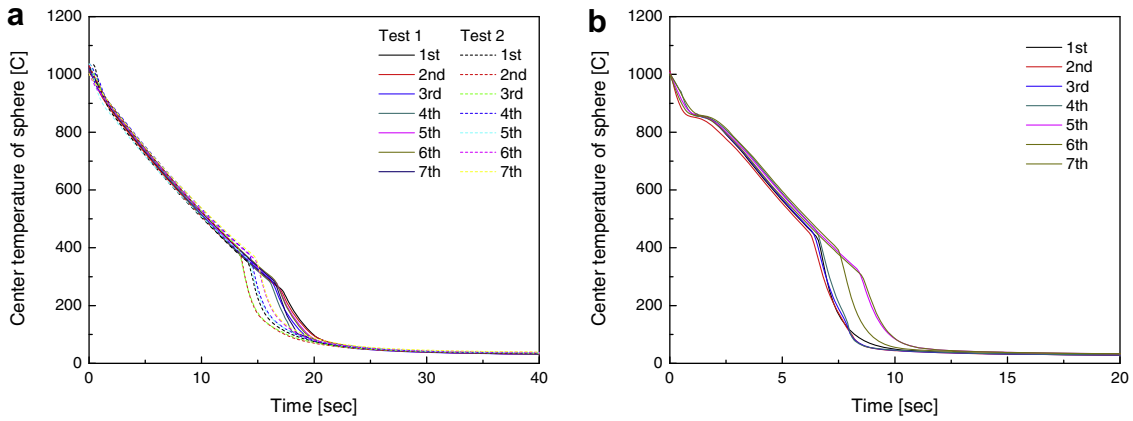

Fig. 8. Quenching curves for SS (a) and Zry (b) spheres in pure water at 70 °C subcooling.

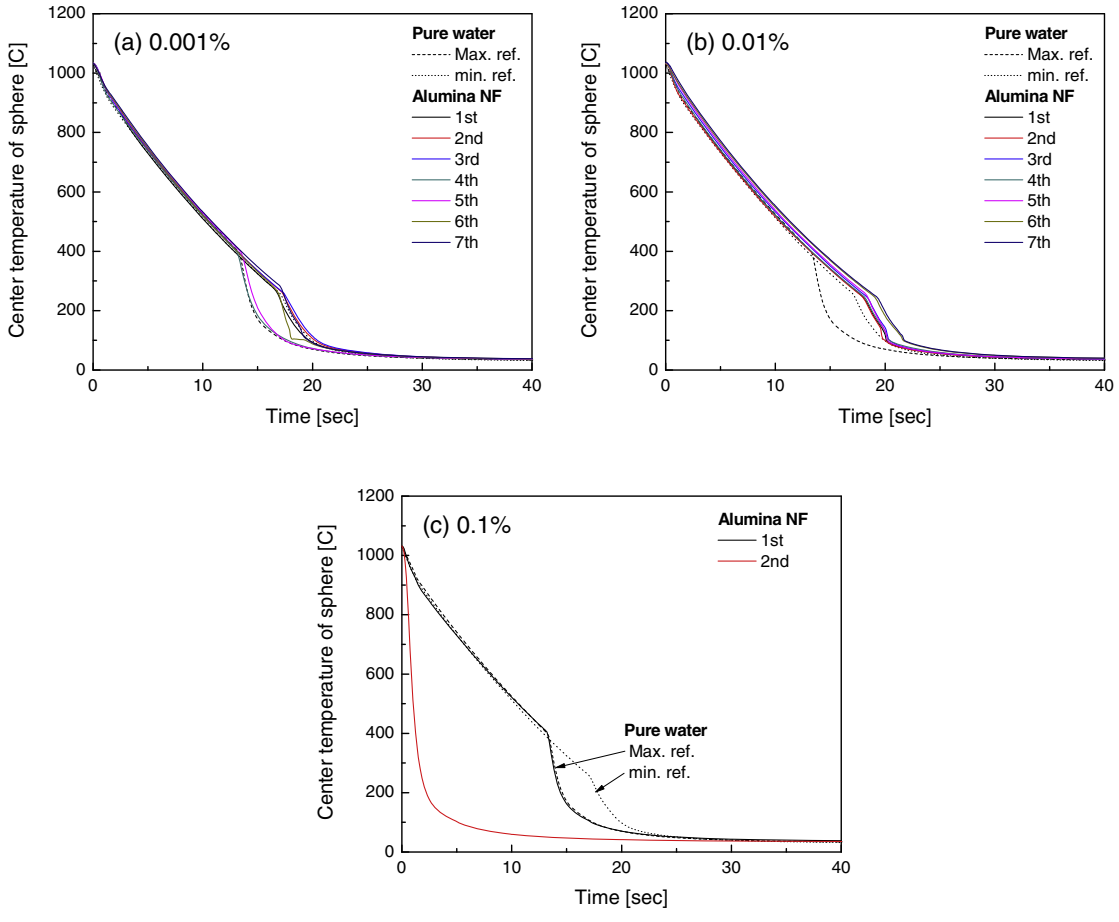

Fig. 9. Quenching curves for SS sphere in alumina nanofluids of (a) 0.001, (b) 0.01, and (c) 0.1 vol% at 70 °C subcooling. Photographs show (d) propagative collapse of thin vapor film immediately after immersion of the heated sphere in the 2nd run of 0.1 vol% nanofluid, at t = 0.000, 0.136, 0.451, 0.635, 0.865, 1.128 s, respectively.

low CHF values (~430 kW/m^2) were found also by Xue et al. (2007) in their quenching experiments with a 25-mm diameter nickel-plated copper sphere in a pool of saturated water. Moreover, as noted by Maracy and Winterton (1988), CHF in pool boiling can exhibit a pronounced hysteresis, i.e., it tends to be lower in a cooling experiment (such as quenching) than in a heating experiment.

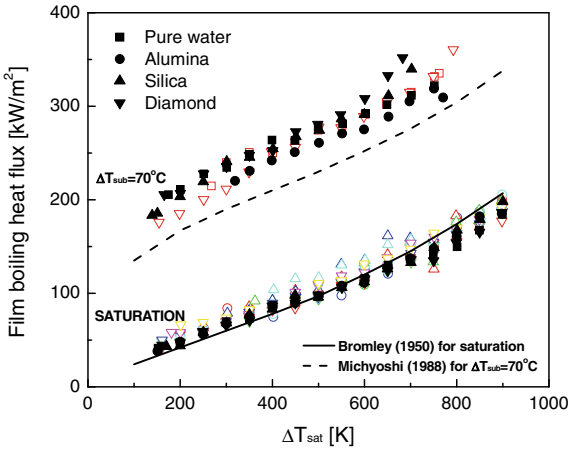

Fig. 10. Film boiling heat flux in pure water and 0.1 vol% nanofluids at saturation and 70 °C subcooling for SS spheres (filled symbol: data for the 1st test; open symbol: data for the 2nd–7th test).

Fig. 11 shows that the boiling curves for the alumina and silica nanofluids on the SS spheres undergo remarkable changes from one repetition to the next. The CHF is significantly enhanced and so is the temperature at which the film boiling region ends. On the other hand, the changes to the boiling curve of the diamond nanofluids are not equally dramatic. The trends for the Zry spheres are very similar to those for the SS spheres, as shown in Fig. E.A.2.

The CHF and MHF parameters extracted from the 0.1 vol% boiling curves for saturated conditions are plotted in Fig. 12. The CHF values significantly increase upon repeated quenching in alumina and silica nanofluids on both SS and Zry spheres. In the SS sphere case, the initial CHF for the two nanofluids is about 450 kW/m^2, which is lower than that of pure water, 580 kW/m^2. However, the CHF of both nanofluids continuously increases from one repetition to the next, and finally reaches a value of 850 kW/m^2, representing a ~50% enhancement above that of pure water, which is consistent with the results shown in various steady state pool boiling experiments with nanofluids (You et al., 2003; Vassallo et al., 2004; Bang and Chang, 2005). On the other hand, the initial CHF for the diamond nanofluid is 620 kW/m^2, higher than the initial values for the other nanofluids and water, but does not increase during the repetitions. As for the MHF-point wall superheat, it considerably increases in alumina and silica nanofluids, i.e., from 150 °C to 300 °C, while it only increases by 30 °C in the diamond nanofluid. A note of caution about the MHF data is in order. As compared to pure water, the alumina and silica nanofluid boiling curves are fairly flat towards the end of the film boiling region, due to early disruption of the vapor film (see Fig. 6d). As such, identification of the MHF point for these nanofluids is challenging and somewhat arbitrary; in Fig. 12 we have reported the MHF wall superheat temperature defined as the temperature at which the slope of the boiling curve undergoes a sudden growth, due to the start of the transition boiling regime.

To simplify the presentation, the boiling curves (and related parameters) for subcooled conditions are not shown here; however, they do exhibit trends qualitatively similar to the boiling curves at saturated conditions, with alumina and silica nanofluids

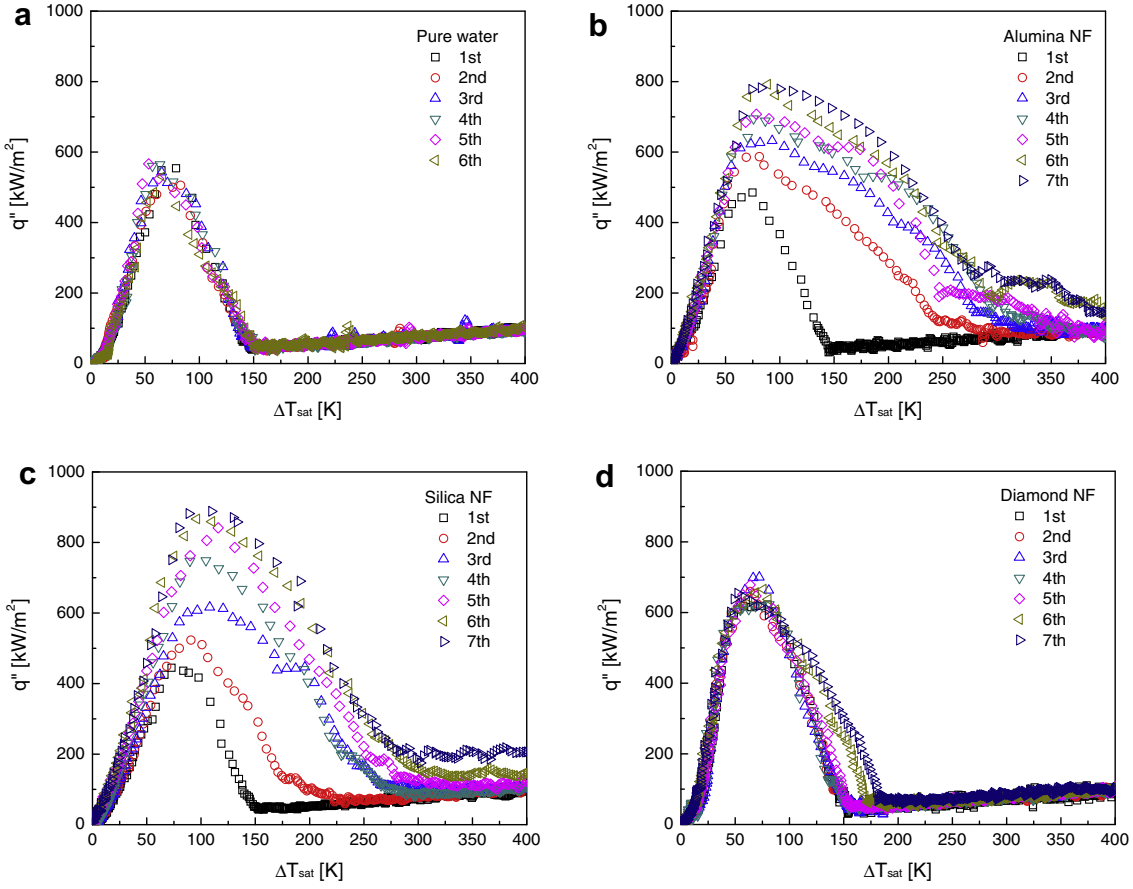

Fig. 11. Boiling curves of (a) pure water, (b) alumina (0.1 vol%), (c) silica (0.1 vol%), and (d) diamond at 0.1 vol% nanofluids for saturated conditions (SS sphere).

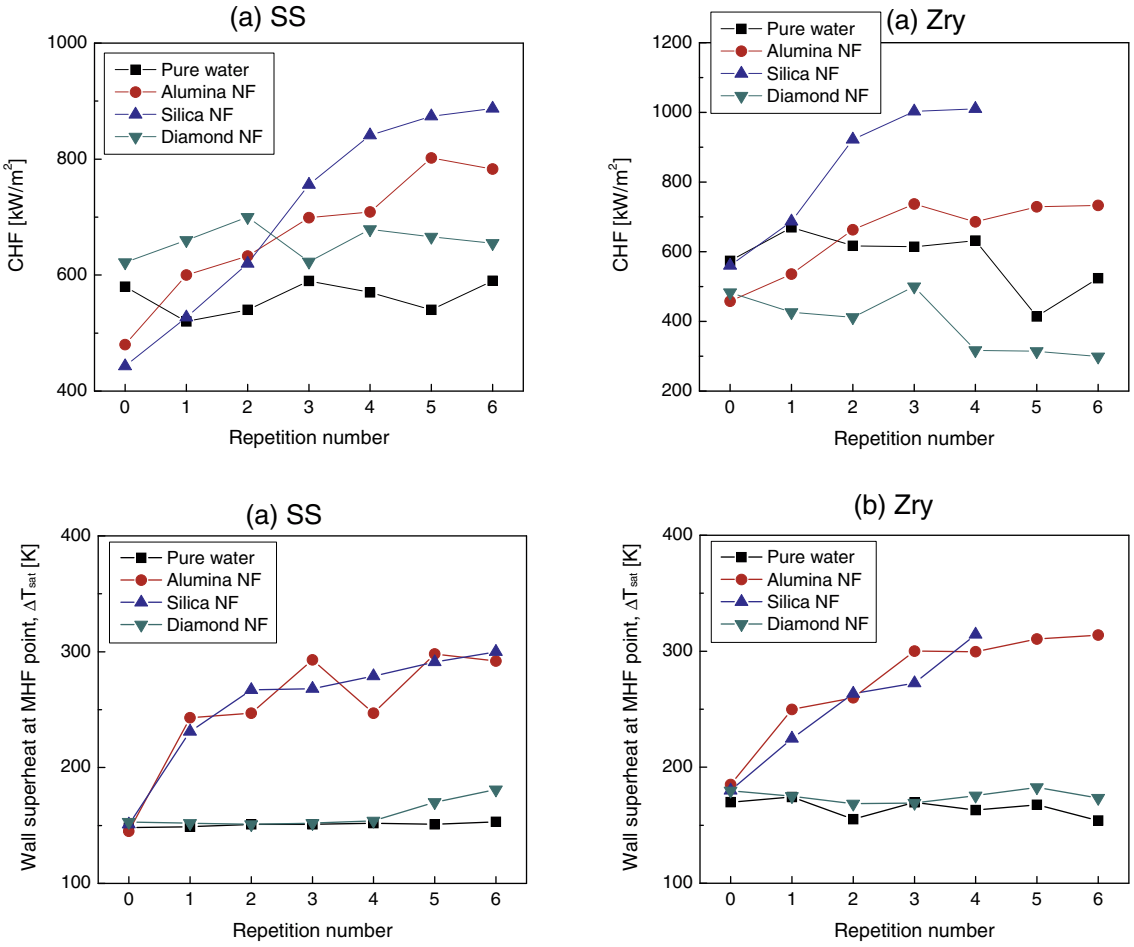

Fig. 12. CHF (a) and MHF-point wall superheat (b) vs repetition number in water and 0.1 vol% nanofluids at saturated conditions (left: SS spheres, right: zircaloy spheres).

again having a higher CHF and MHF than pure water, while diamond shows no significant deviation from the pure water data.

4.3. Nucleate boiling

Figs. E.A.3 and E.A.4 in the Electronic Annex report the nucleate boiling sections of the boiling curves for water and the nanofluids for the SS and Zry spheres, respectively, at saturated conditions. The popular Rohsenow correlation (Rohsenow and Griffith 1956) was also plotted with the data of pure water, for two values of the fluid/surface parameter, i.e., $C_{sf} = 0.015$ (recommended for water/steel by Pioro, 1999) and $C_{sf} = 0.050$, selected to best fit our data. In both cases the correlation agreement with the data is not particularly good. As the Rosenhow's correlation was originally developed for steady-state boiling on flat plates, the reason for its poor performance here could be the spherical geometry and/or the transient nature of the quenching experiments. With respect to pure water (Figs. E.A.3a and E.A.4a), the alumina (Figs. E.A.3b and E.A.4b) and silica (Figs. E.A.3c and E.A.4c) nanofluids exhibit a similar heat flux (for a given wall superheat), while the diamond nanofluid exhibits a somewhat higher heat flux in the SS sphere case (Fig. E.A.3d), and somewhat lower heat flux in the Zry sphere case (Fig. E.A.4d).

5. Data interpretation

The most interesting finding of this study is the remarkable acceleration of the quenching process for spheres repeatedly quenched in nanofluids. Such acceleration cannot be attributed to thermo-physical property changes, as all nanofluid properties are very close to those of water, as explained in Section 2.1. However, SEM inspection of the surface of the spheres reveals that some nanoparticles deposit on the surface during the quenching process in nanofluids (Fig. E.A.5 in the Electronic Annex). It is very plausible to assume that the quenching acceleration in subsequent tests is due to such particle deposition. To test this assumption, spheres previously quenched in nanofluids were quenched in pure water. The quenching curves acquired from these tests are practically identical to those from the last repetition in nanofluids, both at saturated and subcooled conditions (Fig. 13). Therefore, the quenching acceleration must be attributed to the nanoparticles on the surface, not the nanoparticles dispersed in the nanofluid.

But exactly what are the physical mechanisms by which the nanoparticles on the surface affect quenching? The presence of a nanoparticle deposition layer on the surface alters the surface morphology and wettability, and thus can have a significant impact on boiling phenomena. As explained in Section 4, we have observed a significant increase in CHF and, especially, the collapse of the vapor film at a higher temperature, which considerably accelerates the quenching process. The connection between CHF increase and nanoparticle deposition on the boiling surface has been investigated by many and is now fairly well understood. Briefly, the deposition layer enhances the surface wettability, which delays dryout of the hot surface beneath the growing bubbles, thus increasing the CHF (Kim et al., 2006c, 2007a). Very recently, Coursey and Kim (2008) proved that the CHF increase typically observed in

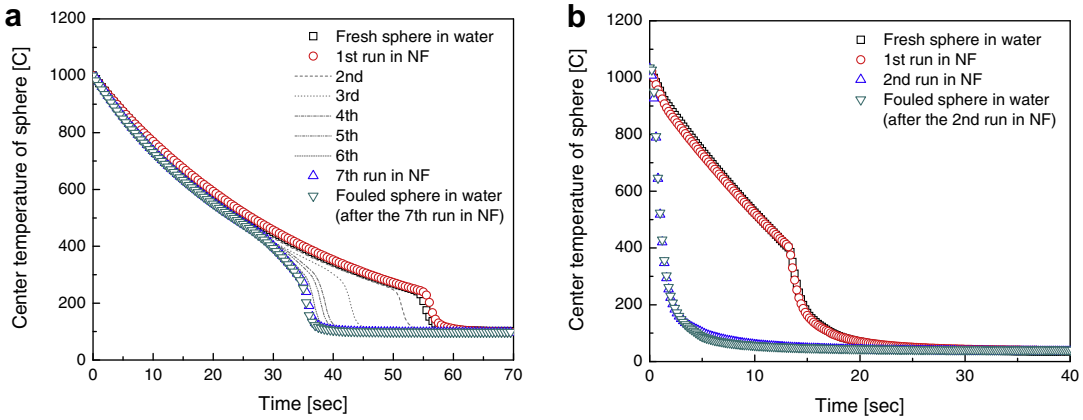

Fig. 13. Quenching curves for fresh and nanoparticle-fouled SS spheres in pure water and 0.1 vol% alumina nanofluids (a) at saturated condition and (b) at 70 °C subcooling.

nanofluid experiments can be reproduced using a properly oxidized surface, and again they attributed such CHF increase to an enhancement of the surface wettability.

On the other hand, the mechanism by which the nanoparticle deposition layer destabilizes the vapor film in film boiling is still unclear. Park et al. (2004) suggested that a roughness increment, due to the nanoparticles accumulated on the surface, destabilizes the thin vapor film (which is typically <100 μm). In our tests the deposited nanoparticles form surface structures with peaks-and-valleys of the order of a few microns (see Fig. E.A.6 in the Electronic Annex). We calculated the vapor film thickness around the sphere during film boiling using the analytical model of Tso et al. (1990), and found that the film thickness at the bottom of the sphere is quite comparable with the length scale of the nanoparticle deposits. Therefore, the thin vapor film could be disturbed by such deposits. This conclusion is corroborated by the observation that the premature collapse of the vapor film in our repeated nanofluid tests consistently initiates at the bottom of the sphere, and then propagates to the whole surface, as seen in Fig. 9d. However surface roughness does not tell the whole story: the nanoparticle deposits in the diamond nanofluid tests produce a significant surface roughness increase, yet the quenching process is not greatly accelerated in those tests.

Another important factor affecting the collapse of the vapor film could be a change of the surface wettability. As shown by Takata et al. (2005) in their experiments with TiO_2-coatings, the higher the wettability of the surface the higher is the MHF-point wall superheat. The vapor–liquid interface in film boiling is always relatively wavy, which can result in short-lived contact points between the liquid and the solid surface, particularly when the surface has a high roughness. If the surface is highly wettable, the liquid can 'stick' to it and spread; bubble nucleation rapidly ensues, which disrupts the vapor film. Now, it is found in the literature that oxides, such as alumina and silica, have higher wettability than metals and diamond, as measured by their static contact angle, i.e., 10–20 ° for pure water on alumina and silica (Kim et al., 2007a,b) vs 70–80 ° for pure water on diamond and steel (Yoshihara et al., 2000; Kim et al., 2006c). These differences in contact angle are expected because oxides, metals and diamond have quite different surface energies. The contact angle was measured for the spheres used in this study, and the results are shown in Fig. 14. Compared to the as-received and water-quenched spheres, the wettability of the spheres quenched in alumina and silica nanofluids is indeed enhanced. However, strangely, the wettability of the spheres quenched in diamond nanofluid is also enhanced significantly.

In conclusion, while it is reasonable to assume that the increased roughness and increased wettability (brought about by the nanoparticle deposition) promote the end of film boiling, the diamond data suggest that there may be some other non-negligible effect, which is however yet to be identified. This is an area for future studies.

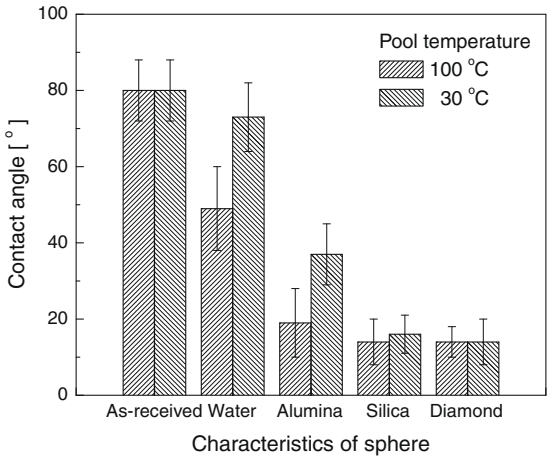

Fig. 14. Contact angles of pure water on the as-received and quenched SS spheres in pure water and nanofluids.

6. Conclusions

The main findings of this study are as follows:

- Film boiling heat transfer in nanofluids is almost identical to that in pure water. That is, the nanoparticles present in the nanofluids have no major effect on the quenching process.
- However, some nanoparticles deposit on the sphere surface during the quenching process, and in *subsequent* quenching tests they can greatly accelerate the end of film boiling, i.e., MHF occurs at a higher wall superheat (by up to 150 °C) than on a fresh sphere. The physical mechanism responsible for such acceleration is likely the destabilization of the vapor film, due to the particle deposits on the surface.
- The effect of liquid subcooling on the acceleration of quenching appears to be very strong. In highly subcooled liquid, the collapse of the vapor film occurs soon after the immersion of the heated sphere into the pool. The data show that, compared to the saturated tests, the thinner vapor film in the subcooled film boiling is more easily destabilized by the particle deposits on the surface.

- An analysis of the boiling curves for the repeated quenching tests of nanofluids shows that CHF is increased from one repetition to the next, due to the growing nanoparticle deposition on the surface.
- The CHF enhancement and the increase of the MHF wall superheat strongly depend on the nanoparticle material used, i.e., the alumina and silica nanoparticles on the surface significantly improve both, while the diamond nanoparticles seem to have no significant effect.

Future work includes a more systematic investigation of the effect of surface characteristics on the quenching process, perhaps through the use of engineered surfaces with controlled wettability and roughness. For the nuclear application, quench tests with rods (vs spheres) are required, as the nuclear fuel geometry is cylindrical. Rodlet tests are underway in our lab and a preview of the data is provided in Appendix B in the Electronic Annex.

Acknowledgements

This research was supported by AREVA, a generous gift from Mr. Doug Spreng, and the Korea Research Foundation Grant funded by the Korean Government (MOEHRD) (KRF-2007-357-D00026). The authors are also grateful to Dr. Michael Pop of AREVA for supplying the zircaloy spheres, Ms. Roberta Concilio Hansson of the Royal Institute of Technology, Stockholm, Sweden, for providing valuable advice on the design of the experimental apparatus, Dr. Roberto Rusconi of the Polytechnic of Milan for providing the SEM images of the alumina and silica nanofluids, Mr. Sung Joong Kim for the nanofluid property measurements, and Mr. Eric Forrest for the DLS measurements.

Appendices. Supplementary data

Supplementary data associated with this article can be found, in the online version, at doi:10.1016/j.ijmultiphaseflow.2009.02.004.

References

Bang, I.C., Chang, S.H., 2005. Boiling heat transfer performance and phenomena of Al_2O_3–water nano-fluids from a plain surface in a pool. Int. J. Heat Mass Transfer 48, 2407–2419.

Bromley, L.A., Leroy, N.R., Robbers, J.A., 1953. Heat transfer in forced convection film boiling. Ind. Eng. Chem. 45, 2639–2646.

Buongiorno, J., Hu, L.W., Kim, S.J., Hannink, R., Truong, B., Forrest, E., 2008. Nanofluids for enhanced economics and safety of nuclear reactors: an evaluation of the potential features, issues and research gaps. Nucl. Technol. 162, 80–91.

Choo, Y.J., Chun, S.Y., Park, J.K., Song, C.H., Bang, I.C., 2008. Experimental study on boiling heat transfer using standard nanofluids. In: Proceedings of the Seventh International Topical Meeting on Nuclear Reactor Thermal Hydraulics, Operation and Safety, Seoul, Korea.

Chupin, A., Hu, L.W., Buongiorno, J., 2008. Applications of nanofluids to enhance LWR accidents management in in-vessel retention and emergency core cooling systems, Paper 8043. In: Proceedings of ICAPP 2008, Anaheim, CA, June 8–12.

Collier, J.G., Thome, J.R., 1996. Convective Boiling and Condensation, third ed. Oxford Science Publications.

Coursey, J.S., Kim, J., 2008. Nanofluid boiling: the effect of surface wettability. Int. J. Heat Fluid Flow 29 (6), 1577–1585.

Kim, H., Kim, J., Kim, M.H., 2006a. Experimental study on CHF characteristics of water–TiO_2 nanofluids. Nucl. Eng. Technol. 38, 61–68.

Kim, H., Kim, J., Kim, M.H., 2006b. Effect of nanoparticles on CHF enhancement in pool boiling of nano-fluids. Int. J. Heat Mass Transfer 42, 2003–2013.

Kim, S.J., Bang, I.C., Buongiorno, J., Hu, L.W., 2006c. Effects of nanoparticle deposition on surface wettability influencing boiling heat transfer in nanofluids. Appl. Phys. Lett. 89, 153107.

Kim, S.J., Bang, I.C., Buongiorno, J., Hu, L.W., 2007a. Surface wettability change during pool boiling of nanofluids and its effect on critical heat flux. Int. J. Heat Mass Transfer 50, 4105–4116.

Kim, H.D., Kim, J., Kim, M.H., 2007b. Experimental studies on CHF characteristics of nano-fluids at pool boiling. Int. J. Multiphase Flow 33, 691–706.

Liu, C., 1995. Film boiling on spheres in single- and two-phase flows. PhD Thesis, University of California, Santa Barbara, CA.

Liu, Z., Liao, L., 2008. Sorption and agglutination phenomenon of nanofluids on a plane heating surface during pool boiling. Int. J. Heat Mass Transfer 51, 2593–2601.

Maracy, M., Winterton, R.H.S., 1988. Hysteresis and contact angle effects in transition pool boiling of water. Int. J. Heat Mass Transfer 31, 1443–1449.

Michyosi, I., Takahashi, O., Kikuchi, Y., 1988. Heat transfer and the low limit of film boiling. In: Proceedings of the First World Conference on Experimental Heat Transfer, Fluid Mechanics and Thermodynamics, Dubrovnik, Yugoslavia, pp. 1401–1415.

Milanova, D., Kumar, R., 2005. Role of ions in pool boiling heat transfer of pure and silica nanofluids. Appl. Phys. Lett. 87, 233107.

Nishio, S., Uemura, M., Sakaguchi, K., 1987. Film boiling heat transfer and minimum-heat-flux (MHF)-point condition in subcooled pool boiling. JSME Int. J. 30, 1274–1281.

Park, H.S., Shiferaw, D., Sehgal, B.R., Kim, D.K., Muhammed, M., 2004. Film boiling heat transfer on a high temperature sphere in nanofluid. In: Proceedings of 2004 ASME Heat Transfer/Fluids Engineering Summer Conference, Charlotte, NC, pp. 1–8.

Pioro, I.L., 1999. Experimental evaluation of constants for the Rohsenow pool boiling correlation. Int. J. Heat Mass Transfer 42, 2003–2013.

Rohsenow, N.M., Griffith, P., 1956. Correlation of maximum heat transfer data for boiling of saturated liquids. Chem. Eng. Prog. Symp. Ser. 52, 47.

Takata, Y., Hidaka, S., Cao, J.M., Nakamura, T., Yamamoto, H., Masuda, M., Ito, T., 2005. Effect of surface wettability on boiling and evaporation. Energy 30, 209–220.

Terai, T., Takahashi, Y., Masumura, S., Yoneoka, T., 1997. Heat capacity and phase transition of zircaloy-4. J. Nucl. Mater. 247, 222–226.

Tso, P.C.P., Low, H.G., Ng, S.M., 1990. Pool film boiling from spheres to saturated and subcooled liquids of Freon-12 and Freon-22. Int. J. Heat Fluid Flow 11, 154–159.

Vassallo, R., Kumar, S., Amico, D., 2004. Pool boiling heat transfer experiments in silica–water nano-fluids. Int. J. Heat Mass Transfer 47, 407–411.

Xue, H.S., Fan, J.R., Hong, R.H., Hu, Y.C., 2007. Characteristic boiling curve of carbon nanotube nanofluid as determined by the transient calorimeter technique. Appl. Phys. Lett. 90, 184107.

Yoshihara, S., Shinozaki, K., Zenbayashi, T., Morino, S., Shirakashi, T., Hashimoto, K., Tryk, D.A., Fujishima, A., 2000. Nature of the photographic diamond surface phenomenon on boron-doped diamond. Electrochim. Acta 45, 3375–3378.

You, S.M., Kim, J.H., Kim, K.H., 2003. Effect of nanoparticles on critical heat flux of water in pool boiling heat transfer. Appl. Phys. Lett. 83, 3374–3376.

Zhou, S.Q., Ni, R., 2008. Measurement of the specific heat capacity of water-based Al_2O_3 nanofluid. Appl. Phys. Lett. 92, 1–3.